RESEARCH ARTICLE
SPACE PHYSICS

Earth and Planetary Physics
2: 538–547, 2018
doi: 10.26464/epp2018052

A study on the energetic electron precipitation observed by CSES

YaLu Wang[1*], XueMin Zhang[1*], and XuHui Shen[2]

[1]Institute of Earthquake Forecasting, China Earthquake Administration, Beijing 100036, China;

[2]Institute of Crustal Dynamics, China Earthquake Administration, Beijing 100085, China

Abstract: High energy particles are the main target of satellite space exploration; particle storm events are closely related to solar activity, cosmic ray distribution, and magnetic storms. The commonly seen energetic particle (electron) precipitation anomalies include mainly the inner and outer Van Allen radiation belts, the South Atlantic Anomaly, and the anomalous stripes excited by artificial electromagnetic waves. The China Seismo-Electromagnetic Satellite (CSES), launched in February of 2018, provides a platform for studying ionospheric particle disturbances. This paper reports the first studies of electron precipitation phenomenon based on high energy particle data from the CSES. We find that the global distribution of electron fluxes in the low energy band (0.1–3 MeV) can relatively well reflect the anomalous precipitation belt, which is consistent with results based on the DEMETER satellite, indicating that the quality of the low-energy band payload of the CSES is good. In addition, this paper makes an in-depth study of the electron precipitation belt excited by the NWC artificial VLF electromagnetic transmitter located in Australia, which appears as a typical wisp structure on the energy spectrum. The magnetic shell parameter *L* corresponding to the precipitation belt ranges from 1.44 to 1.74, which is close to the *L* value (~1.45) of the NWC transmitter; the energy of the precipitation electrons is between 100 keV and 361.57 keV, among which the precipitation of 213.73 keV electrons is most conspicuous.

Keywords: CSES satellite; VLF; Electron precipitation; DEMETER satellite; *L* shell.

Citation: Wang, Y. L., Zhang, X. M., and Shen X. H. (2018). A study on the energetic electron precipitation observed by CSES. *Earth Planet. Phys.*, *2*(6), 538–547. http://doi.org/10.26464/epp2018052

1. Introduction

The electromagnetic field, particle density, and temperature, as well as the energetic particle flux in the space, may change to a certain extent before and after an earthquake; the changes of all these parameters associated with ionospheric disturbances have attracted much attention from researchers specializing in seismic electromagnetics (Zeng ZC et al., 2009; Li XQ et al., 2010; Zhu T and Wang LW, 2011; Zhang XM et al., 2010a, b, 2011, 2012a, b; Huang JP et al., 2010; Wan JH et al., 2012). Among these quantities the high-energy particle disturbance is mostly affected by electromagnetic waves, which can cause pitch angle scattering via wave-particle interaction. Initially the studies on particle disturbance were focused on the mechanism of wave-particle interaction (Koons et al., 1981; Chang HC and Inan, 1983; Berthelier et al., 2006; Parrot et al., 2007; Sauvaud et al., 2008; Gamble et al., 2008; Sidiropoulous et al., 2011). The commonly acknowledged wave-particle interaction is caused by whistler-mode waves, which include plasmaspheric hiss, whistler waves excited by lightning, and VLF electromagnetic waves excited by artificial sources (Abel and Thorne, 1998a, b). Among them, electromagnetic waves in the frequency band 10–25 kHz from ground-based large-power VLF transmitters are an important kind of whistler-mode waves (Imhof et al, 1981, 1983a; Inan et al., 1978, 1984, 2003). With the rapid development of satellite exploring technology, it has been determined from satellite observations that man-made ground sources can definitely cause energetic particle precipitation in space. Some examples are: the EXOS-B satellite observed the 0.3–6.9 keV electron flux anomaly caused by the electromagnetic waves of 0.3–9 kHz from the SIPLE station (Kimura et al., 1983); the low-probability electron flux anomaly created by switching on/off the NPM transmitter was observed by the DEMETER satellite (Inan et al., 2003; Graf et al., 2009); and the DEMETER satellite also observed the electron precipitation belt (*L*=1.4–1.7) correlated to the Australian NWC transmitter (Li XQ et al., 2012).

Therefore, studies on energetic particle anomalies are important for research on electromagnetic wave propagation, particle precipitation and diffusion, the mechanism of sphere-coupling, etc. However, all the aforementioned research achievements are based on foreign satellite data.

Analysis of high-energy particle data from the CSES is reported in this paper, and we present an algorithm developed to realize batch processing and fast mapping of these data. We also present a quantitative study, based on CSES data, of the high-energy particle precipitation phenomenon, supplementing the structural characteristics of the high-energy particle precipitation observed at various satellite altitudes, which demonstrates a scientific basis for carrying out high-energy particle anomaly research based on the CSES platform.

Correspondence to: Y. L. Wang, wangyalu310@163.com
X. M. Zhang, zhangxm96@126.com

Received 16 AUG 2018; Accepted 14 OCT 2018.
Accepted article online 09 NOV 2018.

2. CSES Platform and Its High-Energy Particle Payload

The China Seismo-Electromagnetic Satellite (CSES) was launched on February 2, 2018; it is the first Chinese satellite for the purpose of earthquake research and the first dedicated space-based platform of the Chinese 3D seismological observation system (Wang LW et al., 2016; Shen XH et al., 2018). The satellite carries altogether 8 payloads, including an electric field detector, an induction magnetometer, a high-precision magnetometer, a GNSS occultation receiver, a Langmuir probe, a plasma analyzer, a tri-band beacon, and a high-energy particle detector. The CSES is able to carry out all-weather observations (survey mode) within ±65° of the globe and detailed observation (burst mode) in Chinese territory and 1000 km beyond, as well as in two major earthquake belts of the world (the Circum-Pacific seismic belt and the Eurasia seismic belt), monitoring global physical quantities such as space electromagnetic field and ionospheric plasma density, temperature, and energetic particle energy spectrum, which is expected to be helpful in detecting and measuring earthquake anomaly information. The CSES is designed to operate for 5 years in a sun-synchronous orbit of altitude 507 km with orbit inclination 97°, and revisiting period of 5 days; the longitudinal distance between nearest orbits is about 4.6°.

The CSES is currently undergoing in-orbit test; this paper studies the high-energy particle data acquired during May and June 2018. The high-energy particle detector onboard the CSES consists of three sub-detectors: low energy band, high energy band, and solar X-ray monitor, which can observe the energy spectra of high-energy electrons (2–50 MeV) and protons (15–200 MeV), low-energy electrons (0.1–3 MeV) and protons (2–20 MeV), and solar X-rays (1–20 keV), as well as measure the incidence angle of the charged particle. The high-energy band payload has only one tube with a detecting half angle of 15°, which is used to observe the precipitation of electrons and protons in the high-energy band; while the low-energy band payload is installed on the dark side of the satellite and has 9 tubes with the detecting half angle of 6.5° for odd-number tubes and 15° for even-number tubes, in order to observe the flux of low-energy protons and electrons incident from different angles; the energy resolution is 11.37 keV and the spatial resolution is 1 s.

From May 6 to June 15, 2018, the CSES acquired relatively continuous data of energetic particles. The precipitation of high-energy band electrons (2–50 MeV) and protons (15–200 MeV) and low-energy band protons (2–20 MeV) is rather weak at the altitude of CSES and the observed precipitated particles were thus very few; accordingly, we report mainly CSES data observed in the low-energy electron band (2–20 MeV). During data processing we found that the quality of data from the No.4 tube of the low-energy payload was the best, and the observed electron precipitation phenomenon was also the clearest. Thus, data from the 4th tube, exclusively, was used for the analysis and explication reported in this paper. Data from the other tubes (incidence angles) is not reported here.

3. Global Distribution of Low-Energy Band Electrons

From May 6 to June 15 of 2018 the low-energy band particle payload of CSES acquired altogether 1184 orbits of effective data; 596 orbits are ascending (satellite flies from south to north, corresponding to the night side locally) and the other 588 orbits are descending (satellite flies from north to south, corresponding to the day side locally). Figures 1 and 2 show the global distribution of the low-energy band (0.1–3 MeV) electron flux observed at dayside (descending orbits) and nightside (ascending orbits), respectively. For the convenience of studying the electron precipitation phenomenon, the longitude range is uniformly set to 0°–360°E in this paper; 180°E–360°E corresponds to the western hemisphere.

From the dayside distribution (Figure 1) it can be seen that globally there are mainly three high electron flux anomalies: a planar

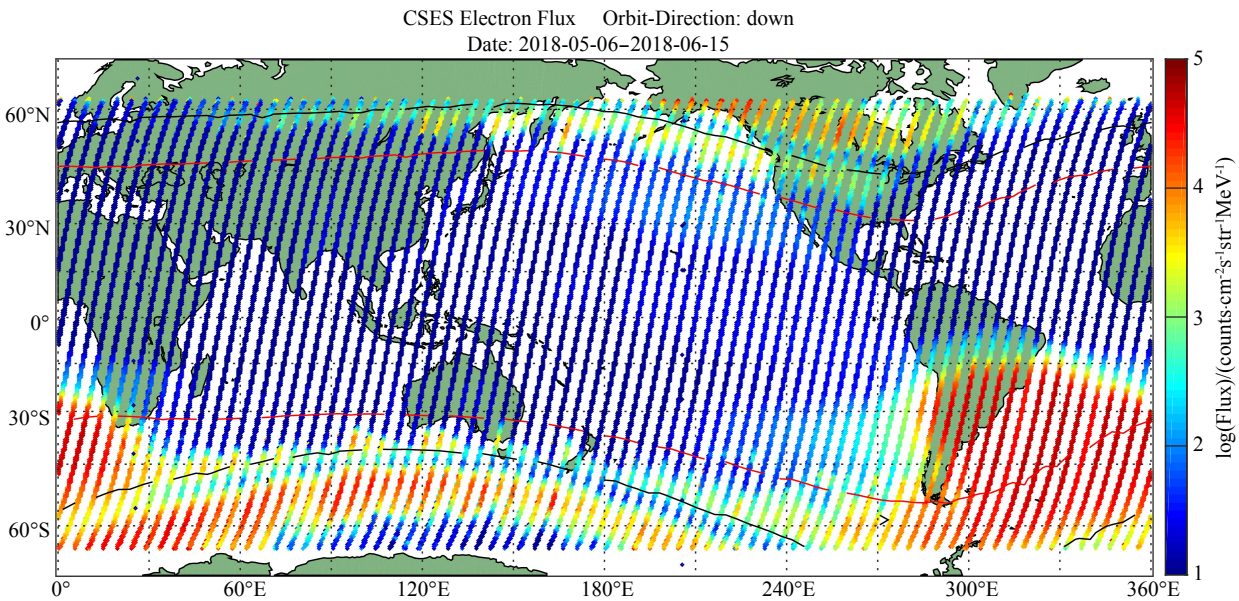

Figure 1. The global distribution of electron (0.1–3 MeV) flux observed by the CSES at dayside (2018-05-06–2018-06-15). Red line: L=1.8; Black line: L=2.9.

anomalous region in the south hemisphere, the longitude of which is between 270°E–30°E and latitude 20°S–50°S, and two easterly-westerly anomaly belts spanning all longitudes at high latitudes in both the south and north hemispheres. The former anomaly corresponds to the South Atlantic Anomaly (SSA); the electron flux is very low in its conjugate region in the north hemisphere. The latter anomalies exist in both southern and northern hemispheres, corresponding respectively to the inner and outer Van Allen radiation belts: the one located at high latitudes (L>2.9) corresponds to the outer radiation belt, while the one located at low latitudes (1.8<L<2.9) corresponds to the inner radiation belt. An arcuate low value region exists in the middle of these two belts, corresponding to the trough (L value about 2.9) of the radiation belt, where the electron precipitation is very weak.

The distribution of low-energy band electrons (0.1–3 MeV) at nightside (Figure 2) is similar to that of dayside (Figure 1). In addition, there are two obvious easterly-westerly electron precipitation anomalies (red ellipses in Figure 2) in the middle latitude regions of the south and north hemispheres, the L values of which are smaller than the inner radiation belt. This phenomenon will be studied quantitatively in Section 4.

In order to verify the quality of CSES energetic particle data, energetic particle data acquired by the DEMETER satellite from May 5 to June 15, 2008, were studied, and the global distribution of the low-energy band (90.7 keV–2.34 MeV) electrons observed at dayside (the time is 10:00 locally) and night-side (the time is 22:00 locally) are shown in Figures 3 and 4, respectively. Comparing Figure 1 with Figure 3 and Figure 2 with Figure 4, it can be seen that the electron precipitation distributions observed by these two satellites are very similar; the low-energy band electron precipitation anomalies observed by the DEMETER satellite are also clearly seen in the CSES results, indicating that the CSES low-energy band electron observation data are stable and of reliable quality. The revisit period of CSES is 5 days, while that of the DEMETER satellite is 13 days, hence the longitudinal orbit spacing of CSES (about 4.6°) is greater than that of DEMETER (about 1.5°), causing the wider inter orbit blanks in the CSES satellite data.

4. Electron Precipitation Excited by Man-Made VLF EM Waves

Many scholars (Sauvaud et al., 2008; Gamble et al., 2008; Li et al., 2012) have studied the electron precipitation phenomenon—the two easterly-westerly stripes at middle latitudes in both the northern and southern hemispheres (Figure 4), which appear as wisp structures in the orbital energy spectrum. The number of electrons with energy between 100 and 600 keV are obviously increased, which tallies with the theory of linear wave-particle interaction. It was inferred that these anomalies can be traced to man-made VLF electromagnetic waves, which may cause electron precipitation in the region above VLF transmitters and their conjugate regions. The scholars compared satellite data observed respectively during the on and off time of the NWC transmitter, and found that when the transmitter was off these anomaly stripes and the wisp structures in the energy spectrum disappeared, but when the NWC transmitter was restarted these anomalies were again observed, straightforwardly indicating that the Australian NWC transmitter had important impact on the formation of these anomaly stripes (Li XQ et al., 2012).

The electron precipitation at dayside caused by man-made VLF electromagnetic waves is relatively weak because the ionosphere absorbs electromagnetic waves strongly at dayside; thus only the night-side phenomenon observed by CSES is studied in this paper. In Figure 2 the longitude of the middle latitude anomaly is approximately between 110°E and 340°E; there are a total of 211 ascending orbits passing through this region from May 6 to June 15 of 2018, the data from which are plotted in Figure 5. The red

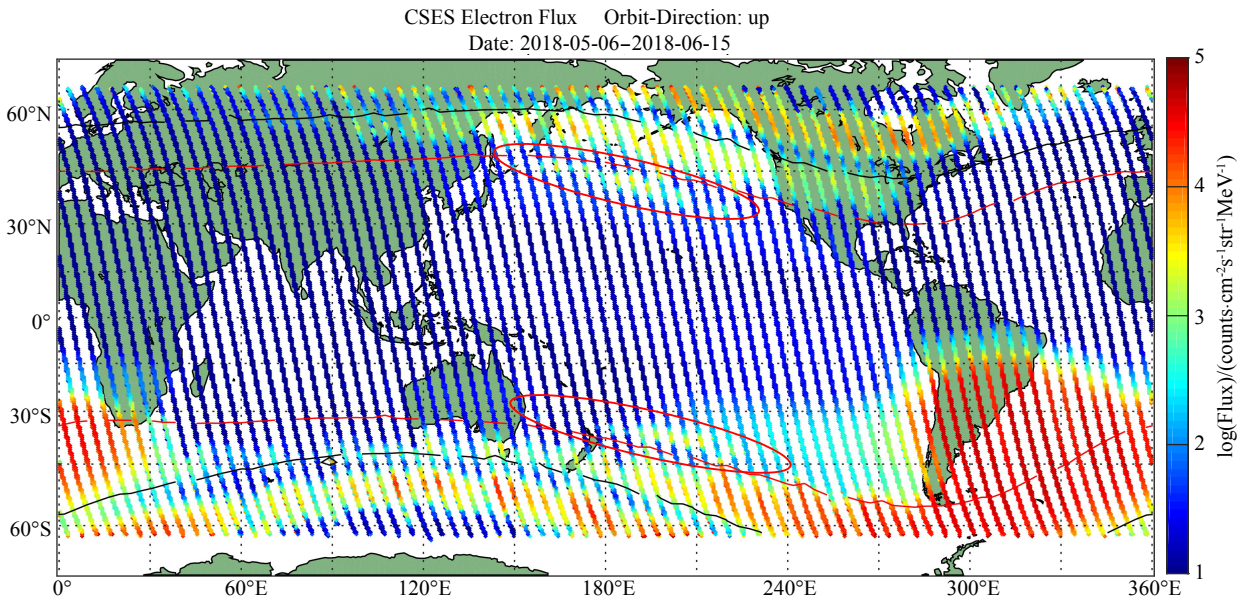

Figure 2. The global distribution of electron (0.1–3 MeV) flux observed by the CSES at nightside (2018-05-06–2018-06-15). Red line: L=1.8; Black line: L=2.9.

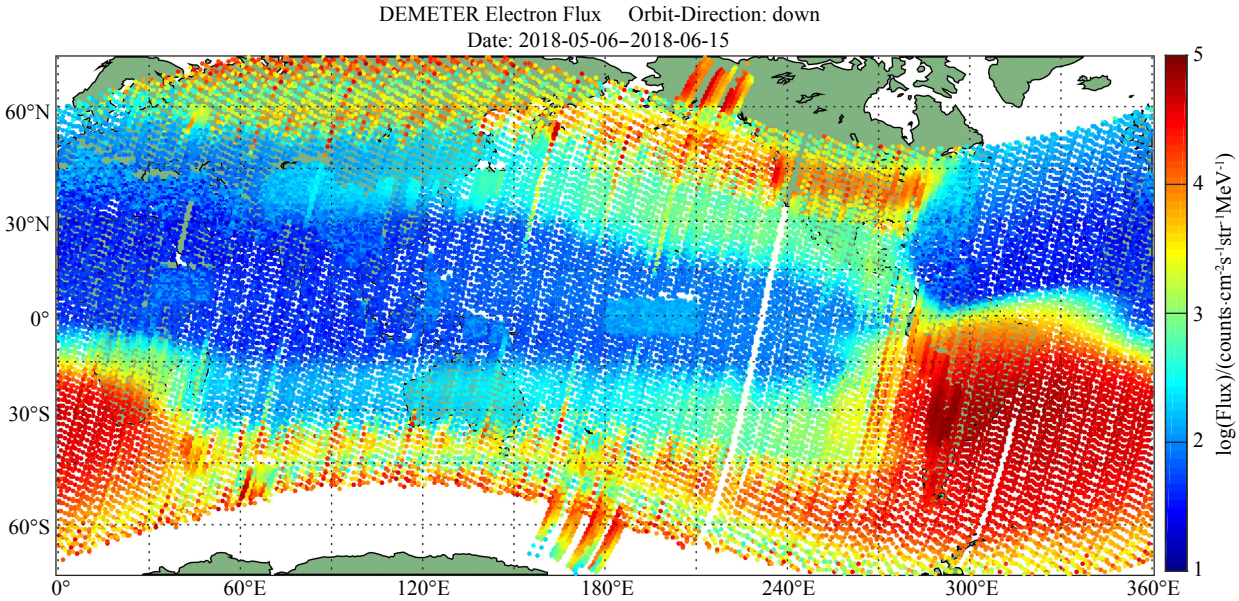

Figure 3. The global distribution of electron (90.7 keV–2.34 MeV) flux observed by the DEMETER satellite at dayside (2008-05-06–2008-06-15).

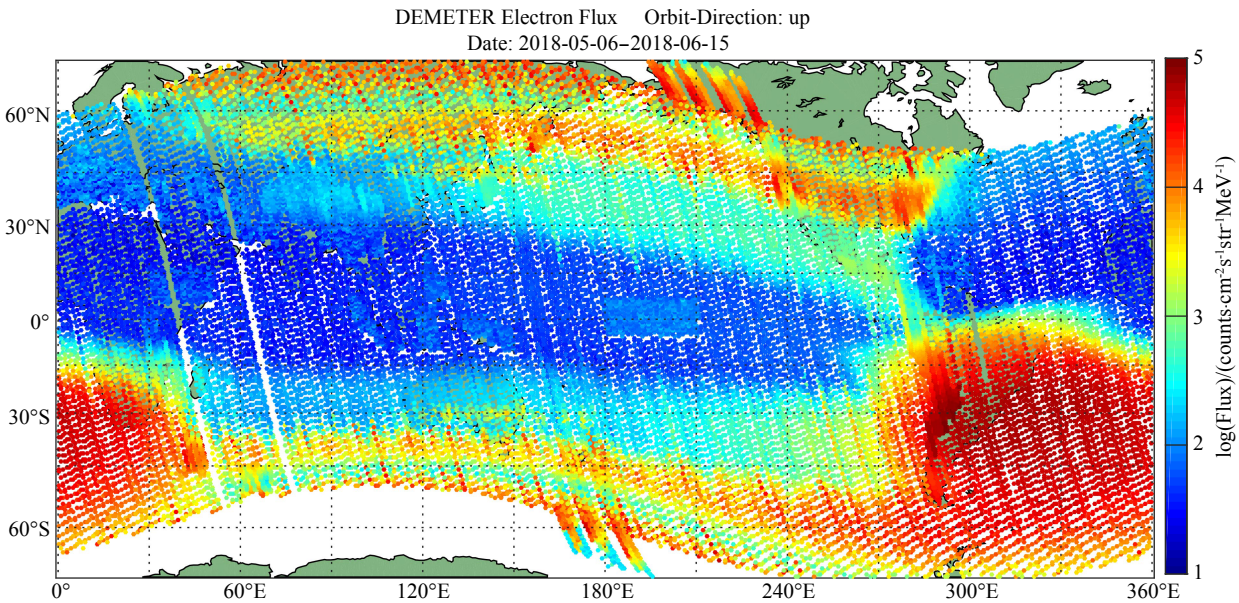

Figure 4. The global distribution of electron (90.7 keV–2.34 MeV) flux observed by the DEMETER satellite at nightside (2008-05-06–2008-06-15).

line in the figure indicates where the corresponding magnetic shell parameter L is 1.4 at the altitude of the CSES, while the black line represents an L value of 1.8. Obviously, the L values corresponding to the belt-like anomaly are approximately between 1.4 and 1.8. The red stars in Figure 5 represent the major VLF transmitters all over the world, and the red diamond is the NWC transmitter in northwest Australia (North West Cape, 19.8 kHz, 1MW, L=1.45). Based on previous research and the location and power of the transmitter, the belt-like electron anomalies between the red and black lines are believed to be caused by the Australian NWC transmitter. For convenience of description, in this paper they are called NWC electron precipitation belts, and the one in the north hemisphere is called the NA region, while the one in south hemisphere is the SA region.

4.1 Wisp Structure

The global distribution of electron precipitation excited by man-made VLF electromagnetic waves displays as a belt-like structure (Figure 5), while a wisp structure in the orbital energy spectrum. Figure 6 shows two typical examples recorded by the CSES during orbit 18131 of June 1 and orbit 18901 of June 6; the left-side figure corresponds to the region NA in Figure 5 and the right-side to region SA; the abscissa is L value, ordinate is energy, and the color scale is electron flux in units of $cm^{-2}s^{-1}str^{-1}MeV^{-1}$. In the range of L=1.5–1.7 both orbits display obvious wisp-like electron precipitation anomaly, i.e., the electron energy decreases with increasing L value, which is hereafter called wisp structure. The wisp structure we report is similar to that of Datlowe published in 2006 (Datlowe, 2006), which he concluded was caused by the first-or-

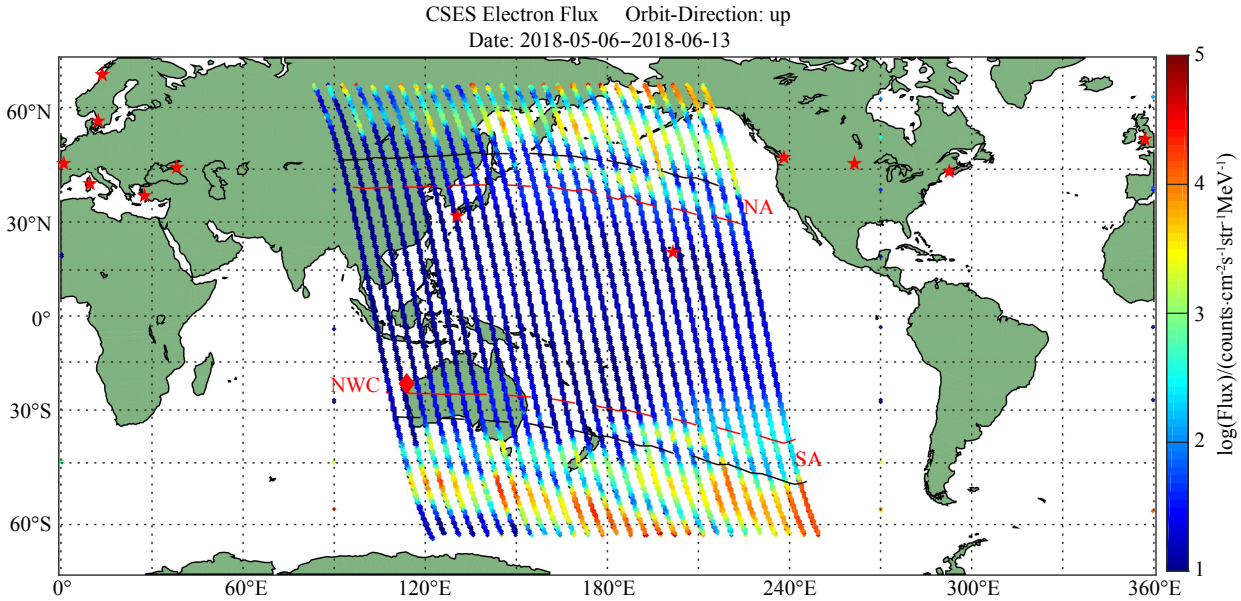

Figure 5. The NWC electron precipitation belt and the conjugate anomaly. Red line: L=1.4; Black line: L=1.8; Red stars: VLF transmitters; Red diamond: NWC Station.

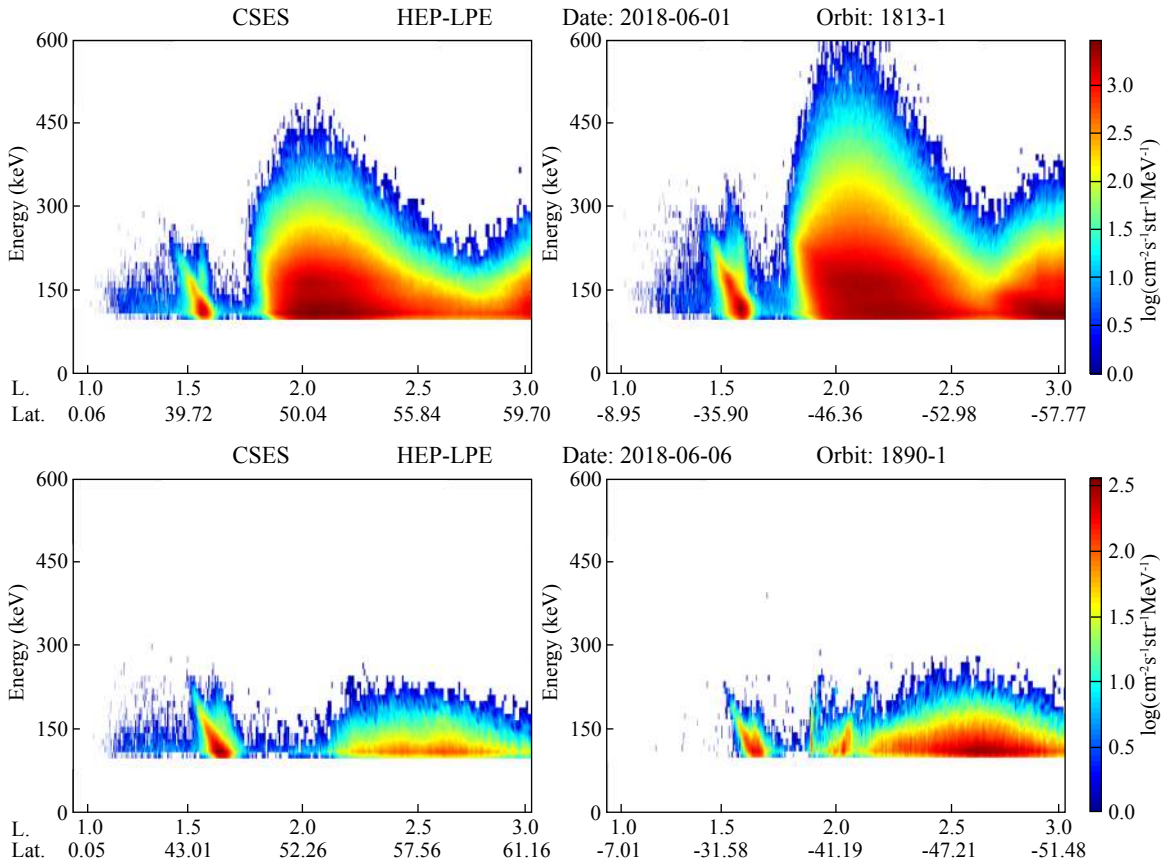

Figure 6. Typical wisp structures observed by the CSES (top panel: orbit 18131; bottom panel: orbit 18901).

der cyclotron resonance of energetic electrons with NWC-transmitted electromagnetic waves in the vicinity of magnetic lines. In orbit 18131 the wisp structure in region SA is more obvious, while in orbit 18901 the anomaly in region NA is more prominent; this indicates that electron precipitation is not identical in regions NA and SA, thus the data in regions NA and SA are discussed especially in the following section.

The wisp structures as shown in Figure 6 appear primarily in orbits to the east of NWC transmitter; however, 12 orbits among the

aforementioned 211 are located at the west side of the NWC transmitter and only rather weak enhancement of electron flux is observed at the approximate *L* values in 3 orbits of these 12 west orbits; moreover the enhancement can be seen only in region SA (Figure 7). Although this characteristic differs from the typical wisp structure, it is believed that this weak enhancement, too, is caused by the NWC transmitter (Gamble et al., 2011) because of its closeness to the NWC transmitter (within 5° on the west side of NWC).

4.2 A Comparison of Regions NA and SA

In order to analyze the spatial distribution characteristics (longitude and *L* value ranges) of the electron precipitation anomalies caused by artificial VLF electromagnetic waves, the precipitation anomaly is firstly defined as 10 consecutive records higher than the background value of the electron flux, which means that the precipitation lasts at least 10 seconds. Here the average electron flux in the *L* range 1.2–1.4 is defined as the background value. The parameters (involving the longitude, the latitude, and the *L* value) of the precipitation anomalies are then obtained for every orbit based on these definitions. Figure 8 shows the histogram of the electron precipitation anomaly number versus *L* value and longitude respectively; the left-side figures are for region NA, the right-side for region SA. The ordinate is the anomaly number and the abscissa is the *L* value and longitude respectively. The *L* value step is 0.01 while the longitude step is 5°.

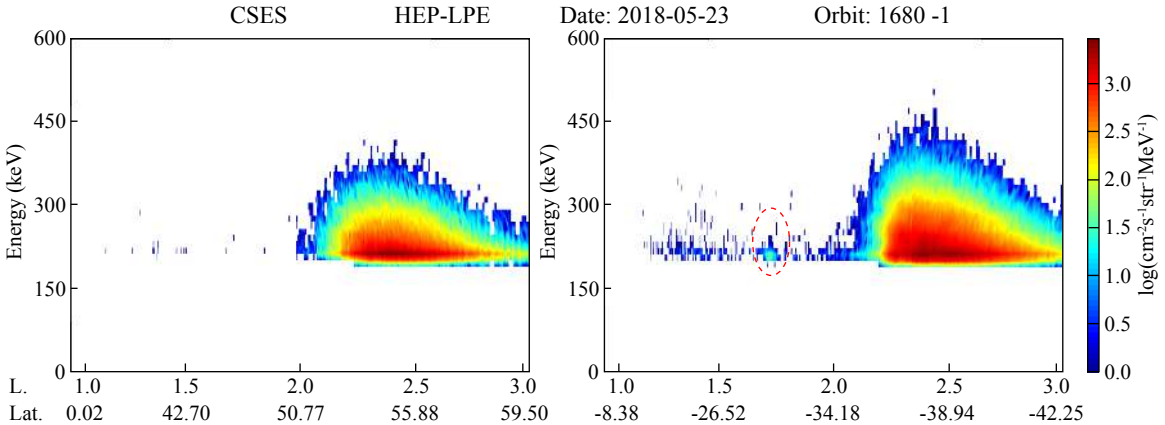

Figure 7. The electron flux enhancement at the west of the NWC station observed by the CSES.

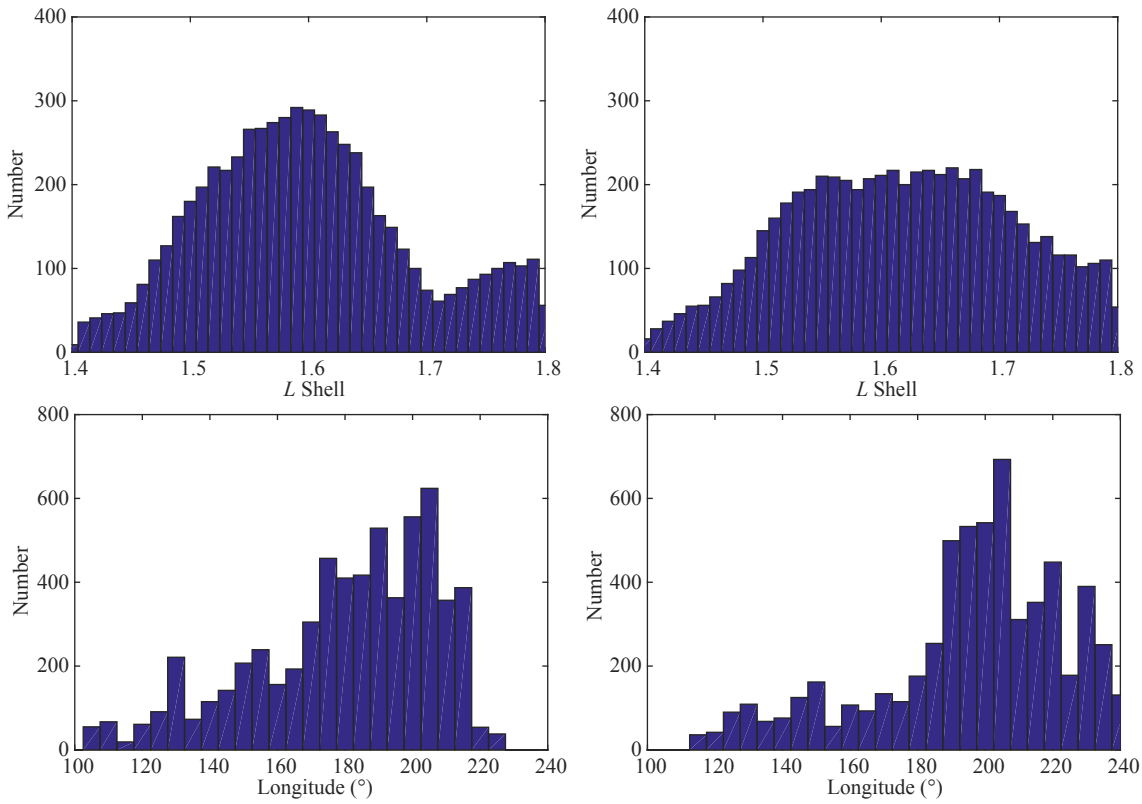

Figure 8. The spatial distribution of the wisp structure in regions NA and SA. Left: Region NA; Right: Region SA.

The *L* and the longitude parameters of the NWC electron precipitation belt in regions NA and SA are listed in Table 1. For region NA (left side of Figure 8) the anomaly number-*L* value plot shows as a Gaussian-like distribution and the *L* value is in the range 1.44–1.71, mainly concentrated between 1.5 and 1.7, reaching the maximum anomaly number at *L*=1.59; the longitude range is 105°E–220°E, mainly concentrated between 170°E and 215°E. For region SA (right side of Figure 8), the anomaly number-*L* plot shows as a trapezoidal shape and the *L* value is in the range 1.47–1.74, also concentrated between 1.5 and 1.7; moreover, the anomaly number almost does not change with *L*; the longitude range is 115°E–235°E, mainly concentrated in 185°E–230°E.

The above result indicates that, regardless of region NA or SA, the longitude range of the NWC electron precipitation belt is obviously shifted to the east of the NWC transmitter (114.15°E). This is because the colliding electrons drift eastward and finally enter the SAA region. The *L* value range of region NA is slightly smaller than that of region SA, which agrees with the conclusion of Li et al. (Li XQ et al., 2012, Figure 10). The *L* values of the NWC electron precipitation belt in this paper are generally smaller than previously reported results, but are closer to the *L* value of the NWC transmitter (~1.45).

4.3 Energy Structure

In Section 4.2 the longitudinal range and *L* value distribution of the NWC electron precipitation belts in the north and south hemispheres were quantitatively analyzed; their energy structure will be studied in this section. For each orbit the quick-view map (Figure 9) is generated. The first subfigure shows the flight trajectory of the satellite and the location of the NWC transmitter, which visually displays the relative position of the orbit and NWC transmitter. The second subfigure shows the electron flux curves in three energy bands (Band 1: 100–600 keV, red; Band 2: 600–1500 keV, blue; Band 3: 1500–3000 keV, green). The third subfigure shows the energy spectra of the orbit; here only the spectrum of Band 1 is given, which will be explained later. The longitude, latitude, and magnetic shell parameter *L* corresponding to the second and third subfigures are given at the bottom of the figure.

It can be seen from the second and third subfigures that the energy spectra of the south and north hemispheres are nearly symmetrical; here the south hemisphere is taken as an example to be explained in detail. In the second subfigure three anomalous re-

Table 1. The geometry of the NWC electron precipitation belts in regions NA and SA

Night-side (ascending orbit)	Min. *L*	Max. *L*	Average *L*	Min. longitude	Max. longitude
NA	1.44	1.71	1.583	105°E	220°E
SA	1.47	1.74	1.6027	115°E	235°E

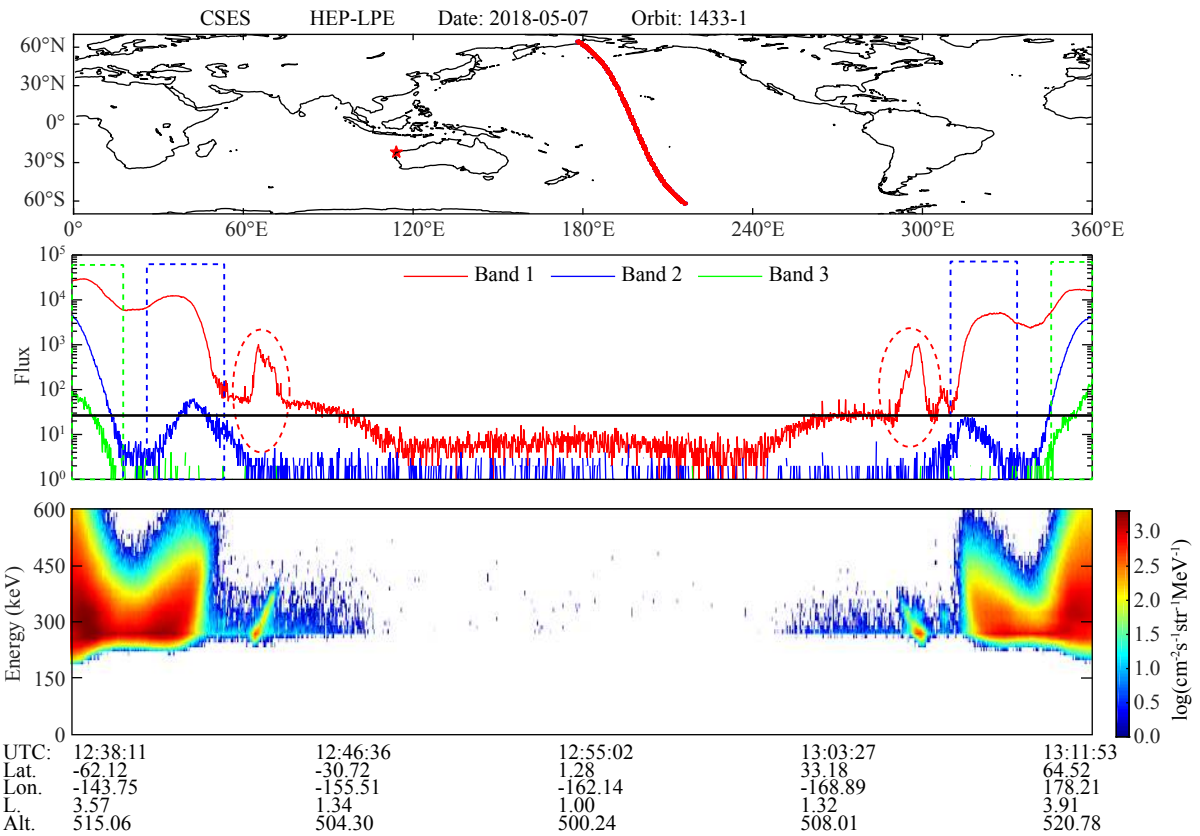

Figure 9. The overviews of the orbit 14331.

gions of high electron flux can be marked out with green, blue, and red frames; among them the green frame corresponds to the Van Allen outer radiation belt, in which the electron fluxes of all three energy bands are enhanced, indicating that in the outer radiation belt electrons in the energy range 0.1–3 MeV can all be observed, but with the increase of energy the electron number gradually decreases. The blue frame corresponds to the inner Van Allen radiation belt, within which only the electron fluxes of Band 1 and Band 2 are enhanced; almost no electrons with energy above 1.5 MeV are observed. The red frame corresponds to the wisp structure in the energy spectrum, i.e., the NWC electron precipitation belt, in which only the electron flux of Band 1 is enhanced, indicating that in the NWC electron precipitation belt mainly the electrons in energy range approximately 100–600 keV collide with the electromagnetic wave and precipitate. Therefore, the maximum electron energy is set to be 600 keV to facilitate the examination of the energy structure of the NWC electron precipitation belt in the third subfigure.

Based on the above analysis, the L value range of the wisp structure, i.e., the NWC electron precipitation belt, is approximately 1.5–1.7, and the L value of the radiation belt is greater than 1.8. In order to compare the energy structures of the NWC electron precipitation belt with its neighboring areas (L<1.4 and L>1.8), the electron flux at L=1.1 is defined as the background value here and the region of L=1.8–2 is designated the radiation belt; the electron flux-energy curves of these three regions are then shown in Figure 10, as well as the ratio of the NWC electron precipitation belt (L=1.5–1.7) and the inner radiation belt (L=1.8–2) to the background value (L=1.1). The average electron flux in the region listed in Table 1 is used in Figure 10 to eliminate random interferences.

It can be seen from Figure 10 that (1) the electron flux of Band 1 (100–600 keV), both in the NWC electron precipitation belt (red curve) and the inner radiation belt (blue curve), is obviously enhanced; (2) in the NWC electron precipitation belt the electron number decreases with increasing energy, and the electron energy is mostly below 1000 keV, especially below 400 keV, while the precipitation of electrons with energy higher than 1000 keV is rather random, as indicated by the curve tail oscillation; (3) in the NWC electron precipitation belt the number of electrons of energy 213.73 keV is the largest; there are three other electron flux maxima respectively at 111.37 keV, 270.58 keV, and 668.63 keV; (4) according to the ratios to the background value (red curve in the second subfigure of Figure 10), in the NWC electron precipitation belt the electron fluxes in the range 100–361.57 keV are enhanced by about several orders of magnitude—especially near the energy 213.73 keV the enhancement of electron flux is most prominent; (5) compared to the NWC electron precipitation belt, electron fluxes in the energy range 300–623.14 keV are obviously enhanced in the radiation belt (blue curve in the second subfigure of Figure 10), indicating that more electrons of higher energy precipitate with increasing L.

5. Conclusion and Suggestions

The relatively continuous high-energy particle data (lasting more than one month) observed by the CSES were analyzed in this paper to verify the stability and reliability of its low-energy band particle detector, by comparing its data with the global distribution of low-energy band electrons (90.7 keV–2.34 MeV) detected by the DEMETER satellite. In addition, the night-side electron precipitation excited by an artificial VLF transmitter was quantitatively studied. Our findings are:

(1) The electron precipitation anomaly caused by the man-made NWC VLF transmitter is mostly observed to the east of the transmitter, where the NWC electron precipitation belt shows a typical wisp structure on the energy spectrum-orbit plot; to the west and nearby the transmitter this anomaly appears as a weak enhancement of the electron flux and the wisp structure cannot be observed.

(2) Our observation indicates that because of the eastward drift of

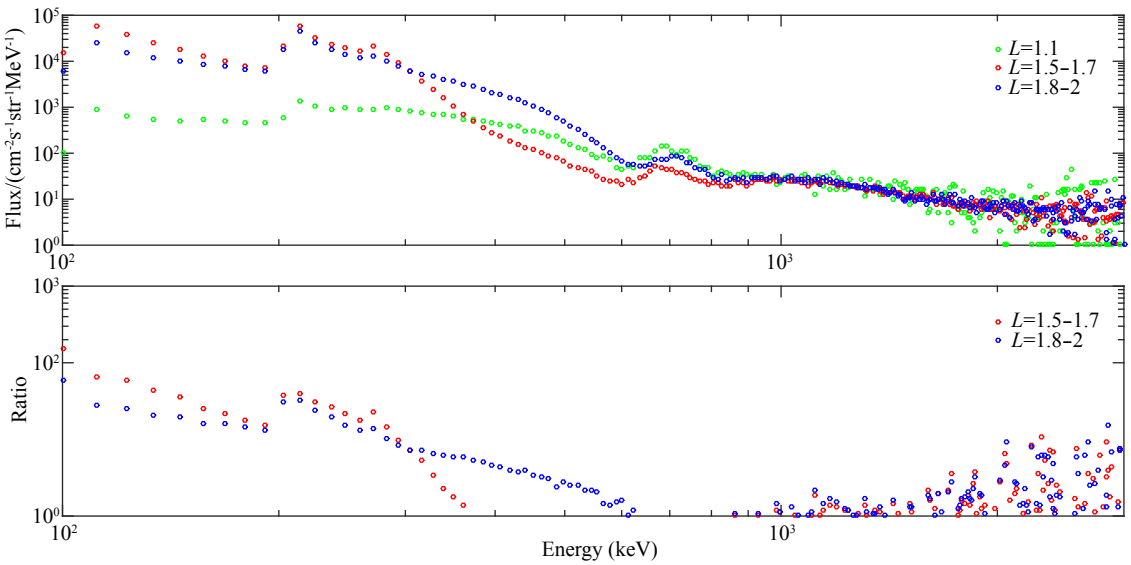

Figure 10. The curves of electron flux and ratio versus energy for the wisp structure and its adjacent domains.

electrons the longitude range of the NWC electron precipitation belt is obviously in the east area, being 105°E–220°E in the north hemisphere and 115°E–235°E in the south hemisphere.

(3) According to the statistics of data concerning the wisp structure (i.e., the NWC electron precipitation anomaly) from 211 ascending CSES orbits, the *L* value range of the NA region is 1.44–1.71 and that of the SA region is 1.47–1.74; these are smaller than the results of previous research, but closer to the *L* value of the NWC transmitter (~1.45).

(4) The energy range of the NWC precipitation belt is 100–361.57 keV; the electron precipitation is most conspicuous at energy 213.73 keV. In the inner Van Allen radiation belt, besides the precipitation of large amount of low-energy (100–300 keV) electrons, the electron number in the energy range 300–623.14 keV is also relatively large.

We obtained the space distribution and the energy structure of the belt-like electron precipitation anomaly excited by ground-based artificial VLF transmitter quantitatively, which are consistent with reported result based on other satellite, demonstrating the reliability of CSES data. However, the duration of CSES data used in these studies is relatively short, and from only one sensor. Also the other variables such as the pitch angle of the electron has not been studied yet, which need to be done in the further work. When the satellite is fully operational, its data is expected to play a major role in future detailed studies of wave-particle interaction and the sphere-coupling mechanism.

Acknowledgment

This paper is supported by NSFC (grant 41674156). We are grateful to the Institute of Crustal Dynamics for providing CSES data, and to the reviewers for their valuable suggestions.

References

Abel, B., and Thorne, R. M. (1998a). Electron scattering loss in Earth's inner magnetosphere-1: Dominant physical processes. *J. Geophys. Res.*, *103*(A2), 2385–2396. https://doi.org/10.1029/97JA02919

Abel, B., and Thorne, R. M. (1998b). Electron scattering loss in Earth's inner magnetosphere-2: Sensitivity to model parameters. *J. Geophys. Res.*, *103*(A2), 2397–2407. https://doi.org/10.1029/97JA02920

Berthelier, J. J., Godefroy, M., Leblanc, F., Malingre, M., Menvielle, M., Lagoutte, D., Brochot, J. Y., Colin, F., Elie, F., … Pfaff, R. (2006). ICE, The electric field experiment on DEMETER. *Planet. Space Sci.*, *54*(5), 456–471. https://doi.org/10.1016/j.pss.2005.10.016

Chang H. C., and Inan, U. S. (1983). Quasi-relativistic electron precipitation due to interactions with coherent VLF waves in the magnetosphere. *J. Geophys. Res.*, *88*(A1), 318–328. https://doi.org/10.1029/JA088iA01p00318

Datlowe, D. (2006). Differences between transmitter precipitation peaks and storm injection peaks in low-altitude energetic electron spectra. *J. Geophys. Res.*, *111*(A12), A12202. https://doi.org/10.1029/2006JA011957

Gamble, R. J., Rodger, C. J., Clilverd, M. A., Sauvaud, J. A., Thomson, N. R., Stewart, S. L., McCormick, R. J., Parrot, M., and Berthelier, J. J. (2008). Radiation belt electron precipitation by man-made VLF transmissions. *J. Geophys. Res.*, *113*(10), A10211. https://doi.org/10.1029/2008JA013369

Graf, K. L., Inan, U. S., Piddyachiy, D., Kulkarni, P., Parrot, M., and Sauvaud, J. A. (2009). DEMETER observations of transmitter-induced precipitation of inner radiation belt electrons. *J. Geophys. Res.*, *114*(A7), A07205. https://doi.org/10.1029/2008JA013949

Huang, J. P., Liu, J., Ouyang, X. Y., and Li, W. J. (2010). Analysis to the energetic particles around the *M*8.8 Chili earthquake. *Seismol. Geol.*, *32*(3), 417–423. https://doi.org/10.3969/j.issn.0253-4967.2010.03.008

Imhof, W. L., Anderson, R. R., Reagan, J. B., and Gaines, E. E. (1981). The significance of VLF transmitters in the precipitation of inner belt electrons. *J. Geophys. Res.*, *86*(A13), 11225–11234. https://doi.org/10.1029/JA086iA13p11225

Imhof, W. L., Reagan, J. B., Voss, H. D., Gaines, E. E., Datlowe, D. W., Mobilia, J., Helliwell, R. A., Inan, U. S., Katsufrakis, J., and Joiner, R. G. (1983a). The modulated precipitation of radiation belt electrons by controlled signals from VLF transmitters. *Geophys. Res. Lett.*, *10*(8), 615–618. https://doi.org/10.1029/GL010i008p00615

Inan, U. S., Bell, T. F., and Helliwell, R. A. (1978). Nonlinear pitch angle scattering of energetic electrons by coherent VLF waves in the magnetosphere. *J. Geophys. Res.*, *83*(B7), 3235–3253. https://doi.org/10.1029/JA083iA07p03235

Inan, U. S., Chang, H. C., and Helliwell, R. A. (1984). Electron precipitation zones around major ground-based VLF signal sources. *J. Geophys. Res.*, *89*(A5), 2891–2906. https://doi.org/10.1029/JA089iA05p02891

Inan, U. S., Bell, T. F., Bortnik, J., and Albert, J. M. (2003). Controlled precipitation of radiation belt electrons. *J. Geophys. Res.*, *108*(A5), 1186. https://doi.org/10.1079/2002JA009580

Kimura, I., Matsumoto, H., Mukai, T., Hashimoto, K., Bell, T. F., Inan, U. S., Helliwell, R. A., and Katsufrakis, J. P. (1983). EXOS-B/Siple Station VLF wave-particle interaction experiments: 1. General description and wave-particle correlations. *J. Geophys. Res.*, *88*(A1), 282–294. https://doi.org/10.1029/JA088iA01p00282

Koons H. C., Edgar, B. C., and Vampola, A. L. (1981). Precipitation of inner zone electrons by Whistler mode waves from the VLF transmitters UMS and NWC. *J. Geophys. Res.*, *86*(A2), 640–648. https://doi.org/10.1029/JA086iA02p00640

Li, X. Q., Ma, Y. Q., Wang, H. Y., Lu, H., Zhang, X. M., Wang, P., Shi, F., Xu, Y. B., Huang, J. P., … Zhao, X. Y. (2010). Observation of particle on space electromagnetic satellite during Wenchuan earthquake. *Chinese J. Geophys.* (*in Chinese*), *53*(10), 2337–2344. https://doi.org/10.3969/j.issn.0001-5733.2010.10.007

Li, X. Q., Ma, Y. Q., Wang, P., Wang, H. Y., Lu, H., Wang, X. M., Huang, J. P., Shi, F., Yu, X.X., … Parrot, M. (2012). Study of the North West Cape electron belts observed by DEMETER satellite. *J. Geophys. Res.*, *117*(A4), A04201. https://doi.org/10.1029/2011JA017121

Parrot, M., Sauvaud, J. A., Berthelier, J. J., and Lebreton, J. P. (2007). First in-situ observations of strong ionospheric perturbations generated by a powerful VLF ground-based transmitter. *Geophys. Res. Lett.*, *34*(11), L11111. https://doi.org/10.1029/2007GL029368

Sauvaud, J. A., Maggiolo, R., Jacquey, C., Parrot, M., Berthelier, J. J., Gamble, R. J., and Rodger, C. J. (2008). Radiation belt electron precipitation due to VLF transmitters: Satellite observations. *Geophys. Res. Lett.*, *35*(9), L09101. https://doi.org/10.1029/2008GL033194

Shen, X. H., Zhang, X. M., Yuan, S. G., Wang, L. W., Cao, J. B., Huang, J. P., Zhu, X. H., Piergiorgio, P., and Dai, J. P. (2018). The state-of-the-art of the China Seismo-Electromagnetic Satellite mission. *Sci. China Technol. Sci.*, *61*(5), 634–642. https://doi.org/10.1007/s11431-018-9242-0

Sidiropoulos, N. F., Anagnostopoulos, G., and Rigas, V. (2011). Comparative study on earthquake and ground based transmitter induced radiation belt electron precipitation at middle latitudes. *Nat. Hazards Earth Syst. Sci.*, *11*(7), 1901–1913. https://doi.org/10.5194/nhess-11-1901-2011

Wan, J. H., Wang, F. F., Shan, X. J., and Yan, X. X. (2012). Preliminary application of energetic particle on DEMETER Satellite in Wenchuan earthquake. *Progress in Geophys.*, *27*(6), 2279–2288. https://doi.org/10.6038/j.issn.1004-2903.2012.06.002

Wang, L. W., Shen, X. H., Zhang, Y., Zhang, X. G., Hu, Z., Yan, R., Yuan, S. G., and Zhu, X. H. (2016). Developing progress of China Seismo-Electromagnetic Satellite project. *Acta Seismol. Sin.*, *38*(3), 376–385. https://doi.org/10.11939/jass.2016.03.005

Zeng, Z. C., Zhang, B., Fang, G. Y., Wang, D. F., and Yin, H. J. (2009). The analysis of ionospheric variations before Wenchuan earthquake with DEMETER data. *Chinese J. Geophys.*, *52*(1), 11–19.

Zhang, X. M., Liu, J., Shen, X. H., Parrot, M., Qian, J. D., Ouyang, X. Y., Zhao, S. F.,

and Huang, J. P. (2010a). Ionospheric perturbations associated with the *M* 8.6 Sumatra earthquake on 28 March 2005. *Chinese J. Geophys.* (*in Chinese*), *53*(3), 567–575. https://doi.org/10.3969/j.issn.0001-5733.2010.03.010

Zhang, X., Zeren, Z., Parrot, M., Battiston, R., Qian, J. and Shen, X. (2011). ULF/ELF ionospheric electric field and plasma perturbations related to Chile earthquakes. *Adv. Space Res.*, *47*(6), 991–1000. https://doi.org/10.1016/j.asr.2010.11.001

Zhang, X., Shen, X., Parrot, M., Zeren, Z., Ouyang, X., Liu, J., Qian, J., Zhao, S., and Miao, Y. (2012). Phenomena of electrostatic perturbations before strong earthquakes (2005-2010) observed on DEMETER. *Nat. Hazards Earth Syst. Sci.*, *12*(1), 75–83. https://doi.org/10.5194/nhess-12-75-2012

Zhang, X. M., Shen, X. H., Liu, J., Ouyang, X. Y., Qian, J. D., and Zhao, S. F. (2010b). Ionospheric perturbations of electron density before the Wenchuan Earthquake. *Int. J. Remote Sens.*, *31*(13), 3559–3569. https://doi.org/10.1080/01431161003727762

Zhang, Z. X., Li, X. Q., Wu, S. G., Ma, Y. Q., Shen, X. H., Chen, H. R., Wang, P., You, X. Z., and Yuan, Y. H. (2012). DEMETER satellite observations of energetic particle prior to Chile earthquake. *Chinese J. Geophys.* (*in Chinese*), *55*(5), 1581–1590. https://doi.org/10.6038/j.issn.0001-5733.2012.05.016

Zhu, T., and Wang, L. W. (2011). LF electric field anomalies related to Wenchuan earthquake observed by DEMETER satellite. *Chinese J. Geophys.* (*in Chinese*), *54*(3), 717–727. https://doi.org/10.3969/j.issn.0001-5733.2011.03.011